

# MeatSpec-G: Generalized Low-Cost Spectral Imaging for Ubiquitous Meat Fraud Inspection

Yinan Zhu<sup>1</sup>, Haiyan Hu<sup>1</sup>, Baichen Yang, Hua Kang, Shanwen Chen, Qianyi Huang\*, Qian Zhang\*, Fellow, IEEE

**Abstract**—Meat adulteration is a significant problem that can pose health risks economic losses to consumers. Current detection methods are hindered by high costs, limited capabilities, or time-consuming sample preparation, making them only accessible in laboratory tests and can not protect the safety of end-users. This paper introduces MeatSpec, a low-cost and user-friendly system for detecting meat adulteration using spectral imaging, to move the adulteration inspection out of laboratories. MeatSpec employs a multispectral camera to reduce costs while quickly capturing spectral images, but this leads to a decrease in spectral resolution and coverage. To solve this challenge, the system uses spectral reconstruction technology and innovative designs tailored for meat adulteration detection. This includes involving adulteration-related prior information during the reconstruction training phase and incorporating contrastive learning to enlarge the distances among reconstructed samples belonging to various adulteration types. Additionally, we devise distinct feature extractors for different bands based on characteristics of the reconstructed spectra and employ knowledge distillation to mitigate error in full-band reconstructed spectra while capturing features related to adulteration. Further, we extend our system to MeatSpec-G to improve its generalizability to varied adulteration conditions and unknown adulterants. To achieve this, we first propose a feature alignment-based training scheme to reduce the feature gap among samples of diverse concentrations and admixture patterns. Then, we propose a cascaded open-set recognition framework that decouples uncertainty quantification and anomaly feature discrimination, to address the limitations of softmax confidence in detecting distribution shifts and reconstruction artifacts. Experimental evaluations on 347 paired spectral images demonstrate that our system achieves a 91.06% accuracy in detecting multiple adulteration types, merely 7.78% inferior to the expensive professional solution, yet 21.58% superior to the baseline at the same price point. Moreover, our system can generalize to achieve an 88.89% detection accuracy in unknown adulteration conditions with a 27.78% improvement, and an 83.33% detection accuracy for unknown adulterants.

**Index Terms**—Meat Adulteration, Spectral Imaging and Reconstruction

## I. INTRODUCTION

M EAT adulteration is a growing concern with significant health and economic implications. The practice of adul-

<sup>1</sup>Yinan Zhu and Haiyan Hu are the co-first authors. \*The corresponding authors are Qian Zhang (qianzh@cse.ust.hk) and Qianyi Huang (huangqy89@mail.sysu.edu.cn).

Yinan Zhu, Haiyan Hu, Baichen Yang, Shanwen Chen, and Qian Zhang are with the Department of Computer Science and Engineering, Hong Kong University of Science and Technology, Hong Kong (e-mail: yzhusdf@cse.ust.hk; hhuap@connect.ust.hk; byangak@cse.ust.hk; schenfh@connect.ust.hk; qianzh@cse.ust.hk).

Hua Kang is with Noah's Ark Lab, HUAWEI. (e-mail: hkangae@connect.ust.hk)

Qianyi Huang is with the School of Computer Science and Engineering, Sun Yat-sen University, Guangzhou 510006, China (e-mail: huangqy89@mail.sysu.edu.cn).

terating meat products involves substituting animal-derived ingredients, injecting water, and using illegal additives [1], which can cause health risks such as foodborne illnesses, allergic reactions, cancer, and kidney damage [2], [3], [4]. Detecting adulterants in meat is crucial for addressing health risks, tracing the source of adulteration, and managing supply chains. In addition, reports show end-of-chain nodes, like catering and retail, are the most vulnerable victims of food fraud [5], which is in-demanding for adulteration detection solutions that are cost-effective, convenient, and without professional operations.

However, existing solutions can not meet this requirement. High requirements for detection capabilities are required due to the notable similarity in composition between adulterated and unadulterated meat samples [6]. Most methods encounter difficulty in achieving a balance between the high detection capability and reasonable cost of the system. Standard detection methods [7], [8], [9] are expensive and require specialized laboratory settings. Hyperspectral solutions [10], [11], while capable of obtaining accurate results without sample preparation, require complex and expensive equipment (costing over \$10,000). Conversely, some low-cost solutions like electronic noses [12] or image classification [13], [14] exhibit limited detection capabilities to discern in-depth chemical characteristics, may miss the most harmful adulteration problem, e.g., veterinary drugs or antibiotic residues. Currently, there is no consumer-grade system that can detect various meat adulteration.

In this paper, we try to bridge the gap by developing a low-cost and user-friendly system for ubiquitous meat adulteration inspection based on spectral imaging. By minimizing the cost, our system can be deployed in ubiquitous dining scenarios, including schools, catering outlets, or halal households to help users quickly get meat adulteration inspection without professional experience. To accomplish this, we first choose an off-the-shelf low-cost multispectral camera [15], which costs one hundredth of a fine-grained hyperspectral camera, as the hardware equipment to significantly minimize the system expenses. Nevertheless, the decrease in hardware cost leads to a decline in both spectral resolution and spectral coverage range, both of which are essential for efficient meat adulteration detection. Fortunately, we are inspired by the fact that spectral reconstruction (SR) technology can recover fine-grained spectral resolution and extend spectral covering range of limited spectral measurements, such as RGB or multispectral images [16], [17], [18], [19], [20]. This technology presents an opportunity to extend the capability of a low-cost multispectral camera to meet the requirements for ubiquitous meat adulteration detection.

However, applying spectral reconstruction algorithms to

develop a low-cost meat adulteration detection system is not a trivial task. It faces the following challenges: **(1) High Similarity of Multispectral Images.** The resemblance between authentic and adulterated samples, especially those with low adulterant concentration, yields analogous spectral attributes, complicating adulteration detection. The low-cost multispectral camera worsens the problem due to its coarse-grained spectral resolution. However, existing spectral reconstruction algorithms cannot reconstruct distinguishable results between two samples sharing similar or even the same multispectral characteristics. **(2) Full-Band Reconstruction Error.** Since the spectral absorption characteristics of different adulteration types span across diverse wavelengths, it is essential for the system to cover a sufficiently broad spectral range, usually 400-1000nm [10], [11]. However, no low-cost multispectral devices can cover such a wide wavelength range. When applying existing spectral reconstruction algorithm for full-band (*i.e.*, 400-1000nm) reconstruction, the errors and noises in reconstructed data will hinder its usability for adulteration detection. **(3) Lack Spectral Reconstruction Dataset.** Spectral reconstruction algorithms require paired (multispectral images, hyperspectral images) data for training. However, obtaining exactly the paired data is challenging. As the field-of-view (FOV) and focal length of the spectral cameras are different, to cover the same scene, the system should be used at a specific fixed distance and angle, which is impractical to implement physically. Previous methods use opened hyperspectral images (HSI) dataset and subsampled HSI as paired multispectral images (MSI) for training, but this approach can result in different distributions of training and test data, leading to reduced performance during deployment.

To overcome the above challenges, we present MeatSpec, the first consumer-grade spectral imaging system for ubiquitous meat adulteration inspection. Specifically, MeatSpec can distinguish between six common types of adulteration, such as substitution, veterinary drug residues, and additives, and use one of the most common targets in meat adulteration cases, *i.e.*, beef, as authentic samples [21]. MeatSpec solves the above challenges with the following designs. **Firstly**, we propose an application-oriented spectral reconstruction (AOSR) module to restore more distinguishable reconstructed images for the cost-effective multispectral input. Specifically, AOSR involves adulteration related prior information during the SR training phase and incorporates contrastive learning that enlarges the distances among reconstructed samples belonging to various adulteration types (see § III-A). **Secondly**, to suppress noise and error in full-band reconstructed spectra and extract adulteration-related features, MeatSpec proposes a reconstruction-adapted adulteration detection (RAAD) module. RAAD designs distinct feature extractors for different bands according to the error distribution characteristics of the reconstructed spectra, and employs knowledge distillation to align extracted features with the original HSI's features in the latent feature space (see § III-B). Moreover, we extend our system to MeatSpec-G to generalize to dynamic adulteration conditions (see § III-C). **Thirdly**, we collect a dataset comprising 347 paired reconstruction training data through our designed pre-processing pipeline. The pipeline involves

several steps to ensure that the MSI and HSI data are aligned and addresses challenges posed by ambient light influence, resolution differences, and variations in sample location during data collection (see § III-D).

We implement a fully-functional prototype of MeatSpec at a cost of less than \$60. We demonstrate the system's capability in detecting minced beef adulteration. Six common types of adulteration, namely substitution, dye substitution, low-quality meat, water injection, edible additives, and toxic additives are considered. For each type of adulteration, we select various typical adulterants, resulting in a total of 13 different adulterants. Results show MeatSpec achieves a 91.06% accuracy in detecting multiple adulteration types, merely 7.78% inferior to the expensive professional solution, yet 21.58% superior to the baseline at the same price point, demonstrating the effectiveness of the system design. We also verify that MeatSpec is robust to various environmental setups, such as meat size, placement and ambient illumination, and the extended system MeatSpec-G is highly generalizable to dynamic adulteration conditions, such as varied concentrations, admixture patterns or totally unseen adulterants.

In summary, we make the following contributions:

- We develop MeatSpec, the first consumer-grade meat adulteration detection system that can accurately distinguish authentic meat and identify the types of adulteration.
- We propose a novel spectral reconstruction scheme and a classification model that fit the reconstructed spectral images, enhancing the accuracy and reliability of meat adulteration detection.
- We open the dataset [22] of beef adulteration detection with 347 paired HSI and MSI data for 13 different adulterants and design a pipeline for aligning spectral reconstruction training data.
- Experimental results demonstrate MeatSpec's high accuracy in detecting various adulteration types and robustness under various experimental and environmental setups.

**Compared to the MobiCom conference version [23]**, we extend MeatSpec to improve its generalizability to dynamic adulteration conditions. In section II, we introduce the generalizability limitation and challenges of previous MeatSpec model, when facing (1) the varied adulteration conditions of known adulterants, *e.g.*, different concentrations and admixture patterns and (2) the totally unknown adulterants. In section III, we first propose a feature alignment-based training scheme to reduce the feature gap among diverse adulteration conditions, guiding the model to focus on their shared spectral absorption peaks inherent to known adulterants, instead of adulteration condition-dependent noises. Then, we propose a cascaded open-set recognition framework that first detects statistical divergence from training data, then precisely evaluates feature-space positioning to reliably distinguish known from unknown adulteration types, addressing the limitations of softmax confidence in detecting distribution shifts and reconstruction artifacts. These two modules form the core contributions of our extended system MeatSpec-G. In section V, we evaluate the generalization performance of MeatSpec-G on varied adulteration conditions and unknown adulterants. The experimental results demonstrate our methods' effectiveness.

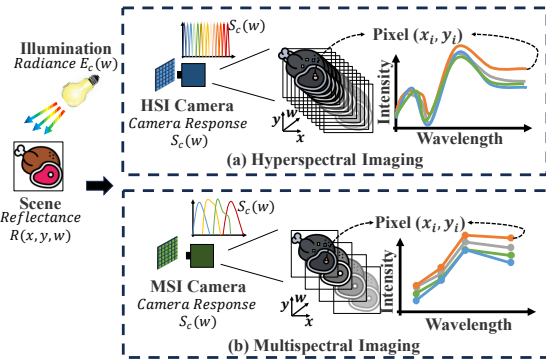


Fig. 1. Various spectral imaging processes of the same meat sample.

Finally, we discuss the future directions for MeatSpec-G's practical application in Section VII.

## II. BACKGROUND AND CHALLENGES

### A. Background

1) *Meat Adulteration Detection with Spectroscopy*: Spectroscopy is a valuable technique for analyzing various properties of substances, including composition, structure, and concentration [24]. In the context of meat adulteration, the chemical profile, such as fatty acid and myoglobin, of each meat species is unique, varying in type and quantity across different tissues [11], [10], [25].

Figure 1 illustrates two typical spectral imaging system, *i.e.*, HSI and MSI, scanning the same meat sample. In principle, a spectral image can be formulated as:

$$I_c(x, y, w) = R(x, y, w)E_c(w)S_c(w), \quad (1)$$

where  $R(x, y, w)$  is the spectral reflectance of the object,  $x, y$  and  $w$  are the width, height and wavelength channel respectively. The spectral reflectance is the key attribute for identifying substances.  $E_c(w)$  is the illumination spectrum, and  $S_c(w)$  denotes the spectral response function, both determined by the hardware parameters of the spectrum acquisition system. Typically, the MSI systems tend to cover small range and have few number of filters than HSI systems due to the cost and size limitation [26], [15]. In contrast, hyperspectral imaging devices are always too expensive, costing over \$10,000, limiting their accessibility to the majority of users [27].

2) *Spectral Reconstruction*: Spectral reconstruction (SR) aims to recover the hyperspectral image (HSI) using a reduced set of measurements or observations, such as MSI, RGB images, or compressed hyperspectral data. The rationale behind hyperspectral reconstruction is based on three key characteristics.

- *Inherent Redundancy*. Neighboring spectral bands in HSI often exhibit high correlation, allowing for leveraging information from adjacent bands to estimate the spectral content of missing or unobserved bands.
- *Sparsity*. HSI tends to demonstrate sparsity in both the spectral and spatial domains, allowing for exploiting this sparsity to reconstruct the full hyperspectral image from a reduced set of measurements.

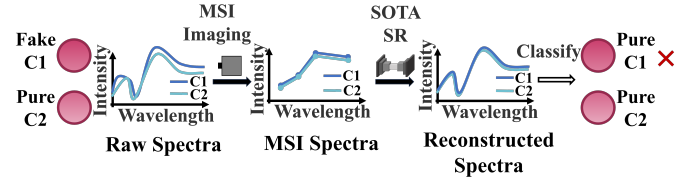


Fig. 2. Illustration of how low-cost MSI imaging makes it harder to tell similar samples apart.

TABLE I  
COMPARISON OF THE CROSS-TYPE VARIANCES (EUCLIDEAN DISTANCES)  
AMONG RAW SPECTRA, MSI SPECTRA, AND RECONSTRUCTED SPECTRA  
USING SOTA SR.

Data	Cross-type Variances
Raw Spectra	0.1951
MSI Spectra	0.1805
Recon (SOTA)	0.1764
MeatSpec	0.2311

- *Spectral Mixing*. HSI can be represented as a linear or nonlinear combination of a limited number of spectral signatures, further facilitating the reconstruction process.

In this way, we can offer a promising solution to overcome the cost barrier associated with acquiring HSI for meat adulteration detection. Currently, lots of deep learning reconstruction algorithms have been proposed and shown good performance in RGB image reconstruction tasks [16], [18], [28], [29].

### B. Challenges

However, the application of these state-of-the-art (SOTA) SR algorithms for meat adulteration detection may face challenges when it comes to reconstructing accurate spectra for similar substances. We conduct comparison experiments using a SOTA spectral reconstruction algorithm, named AWAN [16] to illustrate the problems.

(1) **High Similarity of Multispectral Images**. As we mentioned before, the similarity in composition (*e.g.*, fatty and myoglobin) between adulterated and authentic meat samples is the main challenge in the detection of meat adulteration [6]. The use of low-cost multispectral cameras exacerbates the challenge. As shown in Figure 2, when using a low-cost multispectral device to capture spectral images of similar samples  $C1$  and  $C2$ , the camera can only capture a limited number of spectral bands, resulting in coarse-grained spectra lacking detailed information. Within these limited spectral bands, the MSI spectra of authentic meat and adulterated samples may look further similar or even identical.

Unfortunately, previous SR algorithms can not solve this problem. The rationale of the spectral reconstruction is to learn a one-to-one mapping from paired (MSI, HSI) for the same scene. Therefore, for two different HSIs sharing similar or even the same MSI, the SR algorithm can hardly restore the subtle differences present in the original HSIs, making the reconstructed spectra difficult to distinguish between adulterated and authentic meat. Table I shows the Euclidean distances between different adulteration classes of original HSIs, cost-effective MSIs, and spectral images reconstructed using the existing SOTA SR algorithm in our meat adulteration

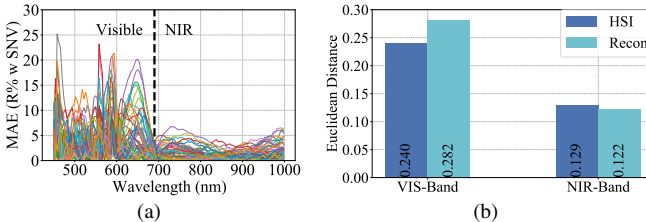


Fig. 3. (a) Reconstruction error of average spectra after SNV. Each color corresponds to one sample. (b) Comparison of the cross-type variances between the original HSI and reconstructed HSI in the visible and near infrared bands.

TABLE II

COMPARISON OF RECONSTRUCTION ERROR BETWEEN SIMULATED MSI AND REAL MSI USING MODEL TRAINED ON SIMULATED MSI DATA.

Data	RMSE	MRAE
Simulated Test MSI	0.0095	0.0234
Real Test MSI	106.71	268.52

dataset [22]. We can find that low-cost MSI imaging and the existing SR algorithm both narrow the distance between different types of adulterated samples.

**(2) Full-Band Reconstruction Error.** Since the spectral absorption characteristics of different adulteration types span across diverse wavelengths, it is essential for the system to cover a sufficiently broad spectral range, *i.e.*, 400-1000nm. Thus, we conduct full-band spectral reconstruction and utilize the reconstructed HSI data for adulteration detection. However, most previous models for meat adulteration detection utilize the pure HSI data as input [11], [30], rather than constructed HSI. Accordingly, these models do not consider the following characteristics of reconstructed HSI data. First, due to the reconstruction error, reconstructed HSI exists more spectral-spatial noises and useless information than pure HSI. Second, since our MSI data does not cover the visible band, it's hard to accurately reconstruct hyperspectral images in the visible band (see Figure 3(a)). These errors and noises in the reconstructed data will hinder its usability for adulteration detection. Thus, previous models cannot directly adapt to our reconstructed HSI data and will perform bad. Moreover, we observe that the reconstructed spectra has large cross-type variances inside the visible band (see Figure 3(b)), which differs from the original HSI.

**(3) Lack Spectral Reconstruction Dataset.** In principle, the spectral reconstruction algorithm needs to obtain paired MSIs and HSIs under the same scene, *i.e.*, having the same  $R(x, y, w)$ . However, obtaining exactly the same  $R(x, y, w)$  using the two systems is challenging. As the field-of-view (FOV) and focal length of the two systems are different, to cover the same scene, the system should be used at a specific fixed distance and angle, which is impractical to implement physically. The previous reconstruction works utilize known response curves of RGB cameras to simulate training RGB data from HSI [16], [31]. However, there is no open response curves library of MSI devices and we can not access the response curve of an off-the-shelf MSI device. We simulate several response curves using the Gaussian distribution as referred to [32]. However, simulation can not restore the MSI data acquisition process, such as MSI detector response, dark

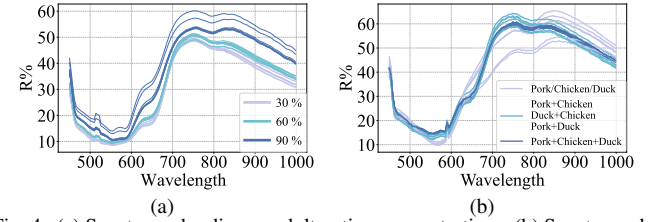


Fig. 4. (a) Spectra under diverse adulteration concentrations. (b) Spectra under diverse admixture patterns.

TABLE III

COMPARISON OF THE FEATURE SIMILARITY (COSINE SIMILARITY) BETWEEN KNOWN AND UNKNOWN ADULTERATION CONDITIONS OF THE SAME ADULTERANTS, USING MEATSPEC AND MEATSPEC-G.

Solution	Concentrations	Admixture Patterns
MeatSpec	0.4158	0.5638
MeatSpec-G	0.6515	0.8101

current noise, *etc.*, resulting in different distribution of training data and test data. As shown in Table II, model training on simulated data significantly reduce reconstruction performance during actual deployment.

**(4) Generalization Gap in Dynamic Adulteration Scenarios.** In addition to the challenges brought by the similarity between adulterated categories and pure meat samples, various complex adulteration situations in the real world also pose significant challenges to model design as follows.

- Varied Adulteration Conditions of the Same Adulterants,* including different adulteration concentrations and admixture patterns. As shown in Figure 4, the concentration change of the adulterate brings about a nonlinear spectral shift, and the change of multi-adulterant admixture patterns leads to diverse combinations of absorption peaks in the spectra. These spectral gaps lead to *low feature similarity* of varied adulteration conditions of the same adulterants, using the previous classification models. This low feature similarity makes it hard to precisely classify a sample with an unknown adulteration condition, even if its adulterants are known in the training samples. From Table III, we can find that for the known same-type adulterants, the sample features extracted by the previous classification model in our MobiCom version [23], have a low cosine similarity of less than 0.6 on average when the adulteration concentrations or admixture patterns change. This greatly limits the generalizability of our system in practical usage.

- Unknown Adulterants.* Current approaches, including our original design (the previous classification model in our MobiCom version [23]), operate effectively only within a closed set of pre-defined adulterant categories, but lack the ability to reliably identify samples adulterated with entirely new substances as “unknown” threats, nor can they generate reliable uncertainty estimates. This poses a serious safety risk, as truly harmful novel adulterants may be misclassified into known categories with high confidence. Furthermore, this limitation is exacerbated by the spectral reconstruction process. Driven by the distribution of the training data, the reconstruction algorithm inherently exhibits a smoothing effect, tending to generate spectra that are very similar to the

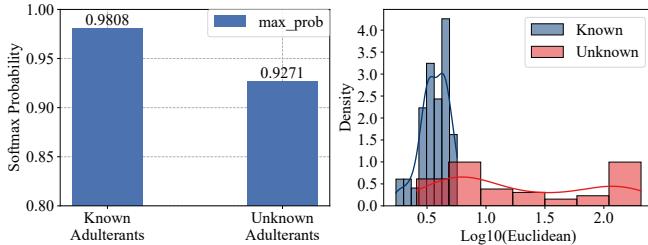


Fig. 5. Left: Average softmax probability of previous classification model on known adulterants (13 types) and unknown adulterants (starch and gelatin). Right: Euclidean distance distribution of known samples and unknowns samples to the class centers.

nearest known profile spectra when dealing with unknown adulterants. This hallucinatory reconstruction masks unique spectral features in the reconstructed spectra, making it difficult for downstream classifiers to distinguish new samples, especially when relying solely on confidence thresholds. As shown in Figure 5, the softmax probability of unknown samples demonstrates similarly high confidence scores to known samples, while the Euclidean distance between unknown samples and known class centers exhibits substantial overlap with the distribution of known samples, indicating significant challenges in distinguishing unknown samples. The dual challenges of the closed-set classification paradigm and the distortion of the feature space caused by reconstruction pose a significant obstacle to generalization capabilities.

### III. SYSTEM DESIGN

Figure 6 shows the architecture of our system. The final target of MeatSpec is to restore as much as possible useful information from collected low-quality data to enable accurate meat adulteration detection. In this way, MeatSpec incorporates two modules: application-oriented spectral reconstruction (AOSR in § III-A) and reconstruction adapted adulteration detection (RAAD in § III-B) to process the data collected from cost-effective MSI hardware. We further enhance the generalizability of MeatSpec to dynamic adulteration conditions in § III-C. In addition, we design a novel pipeline to align paired (MSI, HSI) data for model training and collect a dataset comprising 347 paired spectral reconstruction training data (see § III-D).

#### A. Application-oriented Spectral Reconstruction

To address the challenge of high similarity, we need to modify the existing SR algorithm to enable it to capture the subtle differences among similar MSI spectra of different meat categories. To this end, MeatSpec proposes an application-oriented spectral reconstruction model, which introduces application related prior information during the training phase and incorporates contrastive learning to enlarge the distances among reconstructed samples that share similar MSIs inputs. By this approach, the reconstructed spectra can be better discriminated among different categories of meat samples, enhancing the accuracy and reliability of meat adulteration detection. Figure 7 illustrates the structure of our proposed AOSR model. As we can see, the objective of the model

consists of two parts:  $\mathcal{L}_h$  is the reconstruction loss between the reconstructed spectra and ground truth spectra for the same sample, and  $\mathcal{L}_c$  denotes the contrastive loss of the reconstructed spectra among different categories. Two losses are weighted by  $\alpha$  to adjust the balance between different learning objectives.

**Base Reconstruction Model.** We first leverage a SOTA spectral reconstruction algorithm [16] as the backbone of our AOSR model to reconstruct the hyperspectral image  $\hat{R}(x, y, w)$  for the MSI input  $M(x, y, w_0)$ . The purpose of using SR backbone is two-fold, increasing the spectral resolution and extending the spectral coverage. Therefore,  $\hat{R}(x, y, w)$  will have a wider covering range and more number of bands than  $M(x, y, w_0)$  to support meat adulteration detection. We make some simple modifications on [16] to fit our MSI reconstruction task. Firstly, as [16] takes RGB images instead of MSI as input, we modify its input and output size to fit our dataset. Then, since we utilize an off-the-shelf MSI camera, which can not access its camera spectral sensitivity (CSS) parameters, we remove the CSS loss in [16]. After modification, the reconstruction loss of our base model is defined as:

$$\mathcal{L}_h = \frac{1}{M} \sum_{i=1}^M \frac{|\hat{R}^i - R^i|}{R^i}, \quad (2)$$

where  $M$  is the total number of pixels,  $\hat{R}^i$  and  $R^i$  denote the reconstructed and original spectrum of the  $i$ -th pixel for the sample. By minimizing the loss  $\mathcal{L}_h$ , the model can narrow the distance between the reconstructed HSI and real HSI.

**Contrast-based Reconstruction.** After finishing basic reconstruction, we then introduce meat adulteration prior information and exploit contrastive learning into the training phases. Our goal is to enable the model to distinguish between different classes of samples that share similar or the same multispectral features. In light of this, we construct contrastive loss that maximizes the distance of reconstructed HSI among different categories. We use Euclidean distance to measure the distance of the reconstructed HSI between two samples. We then use the introduced adulteration prior information to screen negative samples for each sample. The negative samples are defined as the samples from the categories that are different from the target within one batch. Our contrastive loss is calculated as follows:

$$\mathcal{L}_c = -\frac{1}{B} \sum_{b^-=-1, b^- \neq b}^B \mathbb{1}(y_b \neq y_{b^-}) \sqrt{\frac{1}{M} \sum_{i=1}^M \|\hat{R}_b^i - \hat{R}_{b^-}^i\|^2}, \quad (3)$$

where  $B$  is the batch size.  $\hat{R}_b^i$  and  $\hat{R}_{b^-}^i$  are the  $i$ -th reconstructed pixel of sample  $b$  and sample  $b^-$ .  $y_b$  and  $y_{b^-}$  are the category label of sample  $b$  and  $b^-$ . The function indicates that we only maximize the distance between the target sample  $b$  and the others having different categories within the batch. As a result, contrastive learning enables the reconstruction algorithm to have better distinguishing capability. As depicted in Table I, by using our design, the Euclidean distances between different adulteration classes of reconstructed HSIs improve from 0.1764 to 0.2311. Further evaluation of the

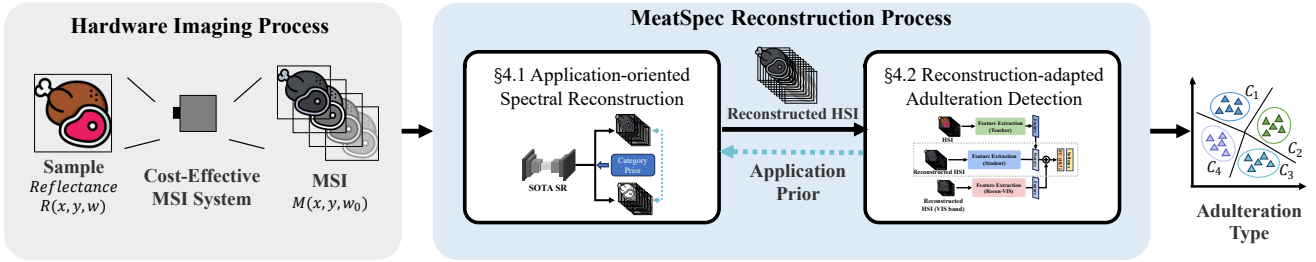


Fig. 6. The system structure of MeatSpec, which consists of two parts: application-oriented spectral reconstruction (AOSR § III-A) and reconstruction-adapted adulteration detection (RAAD § III-B).

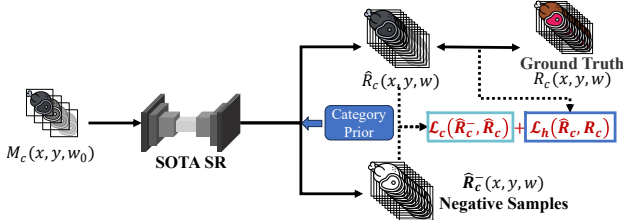


Fig. 7. The working process of application-oriented spectral reconstruction model.

effectiveness of our designed AOSR module is discussed in § V-C1.

### B. Reconstruction-adapted Adulteration Detection

1) *Reconstruction Data Refinement*: To combat the noise and redundant information induced during spectral reconstruction, we consider to refine the reconstructed data as follows. First, we divide each reconstructed hyperspectral image into  $40 \times 40$  patches and conduct average pooling on each patch to reduce the spatial-wise redundant information and accelerate the training process. Next, for spectral-wise denoising, we utilize a mean filter with a window size of 3 to smooth the spectra at each pixel. Then, we apply the common spectral preprocessing method namely standard normalized variate (SNV) on each pixel's spectra to reduce the scattering effect. After these operations, each processed HSI cube with  $40 \times 40$  pixels and 138 channels will be inputted into our designed CNN classifier below.

2) *Reconstruction-adapted CNN Model*: As shown in Figure 8, our adulteration detection model contains three parts: base model, feature distillation and visible information extraction, based on the characteristics of reconstructed data.

**Base Model Design.** Our base model leverages the refined HSI data ( $40 \times 40 \times 138$ ) as input, which adopts three 2D convolutional layers, three batch normalization (BN) layers, three pooling layers and one fully connected (FC) layer. Considering the large noise of reconstructed HSI, the first convolution layer conducts down-sampling to reduce the effect of noise and redundant information. Meanwhile, it does not reduce the spectral-wise dimension, which instead assigns each channel a weight for better feature extraction. Besides, to further avoid overfitting by reconstruction noise, a BN layer and maximum pooling are added after the first convolutional layer. These three layers act as a special denoising module for reconstructed HSI. Then, the output will be inputted to the second convolution layer where we leverage a larger kernel size to extract more global information, because the

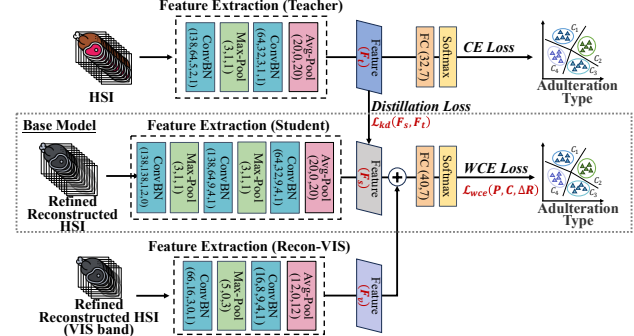


Fig. 8. Model design of reconstruction-adapted adulteration detection.

reconstructed spatial texture may contain incorrect noise and lead to overfitting. So we pay more attention to the global information and spectral dimension. The third convolution layer has the same setting as the second one, which further extracts more fine-grained features. After average pooling to remove the spatial dimension, we can obtain a 32-length embedding, denoted by  $F_s$ .

**Feature Distillation.** As shown in Figure 3(a), it's hard to accurately reconstruct the visible band. But, since the spectral absorption characteristics of different adulteration types are distributed in different bands, we need to utilize the full-band information of the original HSI for effective adulteration detection. To achieve this, we decide to exploit the feature distillation approach. By guiding the feature extractor of reconstructed HSI with that of original HSI, we can transfer the useful knowledge of full band, especially the visible band, for better adulteration detection. Specifically, we regard the base model as the student model and add a branch of teacher model with the original HSI as input. Since the original HSI has little noise, we can reduce its spatial dimension to  $20 \times 20$  pixels after SNV to further accelerate the training. Meanwhile, the teacher model only needs to use two convolutional layers with smaller kernel sizes than that of the student model, and the corresponding BN layers and pooling layers. After training the teacher model, we freeze its model parameters and extract the 32-length embedding before FC layer as the teacher feature, denoted by  $F_t$ . Then, we minimize the gap between the extracted features of the student model ( $F_s$ ) and the frozen teacher model ( $F_t$ ) for feature distillation.

**Visible Information Aid.** Though the visible band is hard to reconstruct, contrastive learning itself can bring some new information inside the reconstructed visible band, due to the usage of negative samples. Figure 3(b) demonstrates that the reconstructed visible band has more information to distinguish

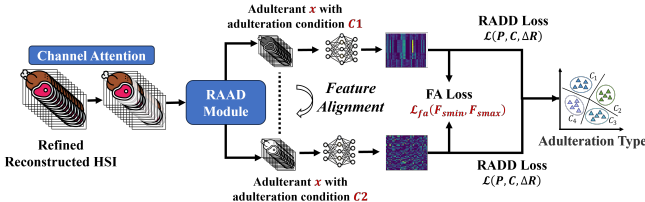


Fig. 9. Feature alignment for enhancing RAAD model generalability.

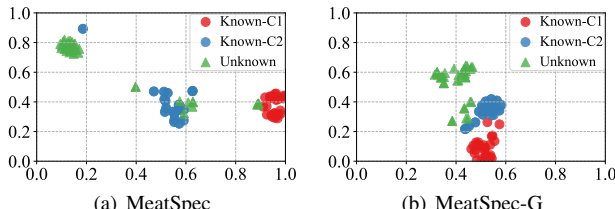


Fig. 10. T-SNE feature distributions of the same adulterants (substitute meat) with varied adulteration conditions, using MeatSpec and MeatSpec-G classification models.

diverse categories than the original visible band. This additional information may help enhance the classification performance. Therefore, we add a branch in our model to extract the additional feature inside the visible band of reconstructed HSI (*i.e.*, the first 66 channels). We extract an 8-length embedding, denoted by  $F_v$ , and concatenate it with our distilled feature. Finally, a formed 40-length feature is fed to the FC layer for classification.

**Weighted Loss.** Eventually, the overall loss function for our CNN model consists of a distillation loss  $\mathcal{L}_{kd}$  and a weighted cross-entropy (WCE) loss  $\mathcal{L}_{wce}$  as:

$$\mathcal{L} = \beta \cdot \mathcal{L}_{kd} + (1 - \beta) \cdot \mathcal{L}_{wce} \quad (4)$$

where  $\beta$  is the weight to trade off the strength of feature distillation for different objects. Note that we define a novel weighted cross-entropy loss for our classification task. We observe that different adulteration types have different degrees of reconstruction error. Larger errors may cause greater difficulty to distinguish. Therefore, we compute the average reconstruction error of each adulteration type as its class weight, which is used in cross-entropy loss for better classification performance:

$$\mathcal{L}_{wce} = -\log(P_c) \frac{1}{N_c} \sum_{i=1}^{N_c} \Delta R_i \quad (5)$$

where  $N_c$  denotes the sample number of the  $c$ -th adulteration type,  $\Delta R_i$  denotes the average reconstruction error of  $i$ -th sample and  $P_c$  denotes the classification probability to  $c$ -th class. In this way, the classification model will pay more attention to those classes with poor reconstruction performance. Besides, for the feature distillation, we use MSE loss as the distillation loss to measure the gap distance between the extracted student features and teacher feature, *i.e.*,  $\mathcal{L}_{kd} = \frac{1}{N_F} \|F_t - F_s\|^2$ , where  $N_F$  is 32. The distillation loss is jointly used with cross-entropy loss during training, which ensures the distillation trend towards high classification accuracy. The effectiveness of our designed RAAD module is evaluated in § V-C2.

### C. Generalization to Dynamic Adulteration Conditions

To bridge the generalization gap to dynamic adulteration conditions, we enhance the detection framework with two novel components that explicitly address dynamic adulteration scenarios. These extensions integrate seamlessly with our core RAAD module while introducing targeted mechanisms for varied adulteration conditions recognition and unknown adulterants identification.

#### 1) Feature Alignment for Varied Adulteration Conditions of Known Adulterants:

To address the challenge of generalization gap incurred by low feature similarity of varied adulteration conditions, *e.g.*, different admixture patterns and concentrations, we need to conduct feature alignment to reduce the feature gaps among diverse adulteration conditions of the same adulterants, during model training. The rationale is that, despite the admixture patterns or concentrations are unknown, the spectral absorption peaks of the same adulterants have been seen inside the training samples. By minimizing the feature gap between samples of minimum and maximum concentrations, and that between samples of lowest and highest admixture complexity - which are distinct feature clusters under the classification model in RAAD module (see Figure 10(a)) - the model's output features will be focused on shared spectral absorption peaks inherent to adulterants themselves, instead of adulteration condition-dependent noises. The reason for choosing samples of minimum-maximum concentrations and lowest-highest admixture complexity, is due to these samples' largest feature gap under all combinations of the spectral absorption peaks. Through this feature alignment approach, the model generalizability to varied unknown adulteration conditions will be much improved, with closer feature clusters and larger feature similarity (see Figure 10(b)). Moreover, we add channel attention weights to the reconstructed data to highlight the shared absorption peaks, further enhancing the alignment performance and preventing overfitting. Figure 9 illustrates the structure of our feature alignment scheme. As we can see, besides the loss  $\mathcal{L}$  proposed in RADD module (§ III-B), the training objective of the enhanced classification model also contains the feature alignment loss  $\mathcal{L}_{fa}$ , which denotes the feature gaps among diverse adulteration conditions, with channel-weighted reconstructed HSI as inputs.

**Feature Alignment.** We employ the Cosine similarity to measure the gaps among different samples' features (*i.e.*,  $F_s$  in § III-B). For each adulterant, let  $S_{min}$  denote the set of samples of minimum concentration and lowest admixture complexity,  $S_{max}$  denote the set of samples of maximum concentration and highest admixture complexity, we try to optimize the model to make the output features of samples in  $S_{min}$  and  $S_{max}$  as close as possible. That is,

$$\mathcal{L}_{fa} = \frac{1}{N_s} \sum_{i \in S_{min}} \sum_{j \in S_{max}} \left( 1 - \frac{F_i \cdot F_j}{\|F_i\| \times \|F_j\|} \right) \quad (6)$$

where  $N_s = |S_{min}| \times |S_{max}|$  denotes the combination quantity and  $F_i$  is  $i$ -th sample's feature. Smaller  $\mathcal{L}_{fa}$  means larger feature similarity. The sets  $S_{min}$  and  $S_{max}$  are obtained within a batch during training.

**Enhanced Loss.** As mentioned, we add a 138-length trainable vector as channel attention weights to the reconstructed HSI ( $\hat{R}$ ), and use this weighted HSI ( $\rho\hat{R}$ ) as CNN model inputs. Thus, combined with the RAAD loss  $\mathcal{L}$ , the overall loss function for training a generalized CNN model finally is

$$\mathcal{L}' = \gamma \cdot \mathcal{L}_{fa}(F(\rho\hat{R})) + \mathcal{L}(\rho\hat{R}) \quad (7)$$

where  $\gamma$  is the weight to balance the feature alignment's strength against overfitting. The feature alignment loss is jointed minimized to make the model converge to a parameter space with high generalizability. The initial values of channel attention weights are uniformly set to one for joint training.

As shown in Fig 10, we conduct a field study of diverse adulteration concentrations, where “Known-C1” means sample features of 10% concentrations and “Known-C2” means sample features of 50% concentrations - both of them are known concentrations in the training samples. After reducing their feature distances using our method, the test sample features of 20% and 40% new concentrations denoted by “Unknown”, will evidently approach more closer to the sample features of known concentrations (10% and 50%). This feature distribution change between 10(a) and 10(b) shows the effectiveness of conducting feature alignment for generalizability improvement. The comprehensive evaluation of this feature alignment module will be presented in § V-E1.

2) *Hierarchical Detection System for Unknown Adulterants:* Detecting new, unseen adulterants presents distinct challenges from generalizing to known contaminants at different concentrations or mixtures. While we enhances the capability of known adulterant distributions through feature alignment, it is still inherently limited to closed-set recognition. To this end, we design a cascaded open-set recognition framework which decouple the challenges of quantifying distribution uncertainty and discriminating anomalies in feature space. This decoupling is critical because softmax confidence fails to reliably capture distributional shifts, while reconstruction artifacts corrupt the very features needed to discern novelty. By first identifying samples exhibiting statistical divergence from training data (Stage 1) and then rigorously evaluating their position relative to known class distributions in a robust feature space (Stage 2), our framework can establish a clear boundary between known and unknown adulteration types.

**Distributional Uncertainty Quantification.** In the first stage, we implement an energy-based detector operating directly on RAAD's pre-softmax logits. The energy function is formulated as:

$$E(x) = -T \cdot \log\left(\sum_{i=1}^K \exp(f_i(x)/T)\right), \quad (8)$$

where  $f_i(x)$  denotes the logit value for class  $i$ , and  $T$  is a temperature parameter scaling score sensitivity. This energy score is negatively correlated with the real data density  $p(x)$ . Therefore, low energy indicates high likelihood under the training distribution (*i.e.*, known categories), while high energy indicates statistical divergence. Unlike softmax probability that is a relative metric that limits the sum to 1, energy can capture absolute model uncertainty and exposes distribution changes caused by new adulterants.

**Feature-Space Anomaly Discrimination.** In the second stage, we employ a class-conditional Mahalanobis discriminator operating in RAAD's teacher-model feature space ( $F(t)$ ) to resolve the critical challenge of reconstruction-induced spectral ambiguity. We deliberately select this space because it maps directly from ground-truth HSI data, thereby avoiding the smoothing distortions inherent in the student pathway's reconstructed features. Specifically, for each known class  $c \in \{0, 1, \dots, K-1\}$ , we compute a class-specific mean  $\mu_c$  as the expectation over training features  $z_t$  and a regularized covariance matrix  $\Sigma_c$ , which is formulated as:

$$\Sigma_c = \frac{1}{N_c - 1} \sum_{i:y_i=c} (z_t^{(i)} - \mu_c)(z_t^{(i)} - \mu_c)^\top + \lambda I, \quad (9)$$

with  $\lambda = 10^{-6}$ , to ensure numerical stability and invertibility while preserving class-specific distribution characteristics. For a candidate feature vector  $z_t$  derived from the first stage's potential ambiguous (*i.e.*,  $E(x) < \tau_{energy}$ ), we compute its Mahalanobis distance to all known classes as:

$$MD_c(z_t) = (z_t - \mu_c)^\top \Sigma_c^{-1} (z_t - \mu_c), \quad (10)$$

where we omit the square root calculation to optimize inference speed without compromising discriminative power. subsequently, we define the smallest Mahalanobis distance as the anomaly score of the sample, *i.e.*,  $OOD\_Score(z_t) = \min MD_c(z_t)$ . Samples are conclusively classified as unknown adulterants if  $OOD\_Score(z_t)$  exceeds the threshold  $\tau_{mah}$ .

The core innovation of this design lies in its intrinsic resistance to spectral reconstruction artifacts. First, Mahalanobis distance exhibits strict affine invariance, where any linear distortion  $\phi(z) = Az + b$  approximating reconstruction-induced warping preserves the metric, guaranteeing consistent novelty detection even when features are projected toward known-class spaces. Second, the covariance term  $\Sigma_c^{-1}$  amplifies deviations orthogonal to dominant feature correlations to expose latent statistical incompatibilities that spectral smoothing attempts to erase. For instance, when a novel adulterant's spectrum is distorted to align with known absorption peaks along primary eigenvectors, residual discrepancies in low-variance directions trigger anomalously high Mahalanobis scores. Thus, by integrating this covariance-aware discriminator with RAAD's existing architecture, which requires zero additional trainable parameters, we transform the reconstruction pipeline's spectral homogenization weakness into a discriminative strength. The thresholds  $\tau_{energy}$  and  $\tau_{mah}$  are jointly calibrated via ROC analysis on validation data, optimizing the trade-off between known-class retention and unknown detection sensitivity. By seamlessly integrating open-set capability into RAAD's existing feature extractor, our solution closes the critical gap between high-fidelity spectral reconstruction and robust unknown threat identification. The effectiveness of this design is evaluated in § V-E2.

During practical usage, MeatSpec-G will first recognize known and unknown adulterants with this framework (§ III-C2) and then employ our enhanced models with feature alignment (§ III-C1) to detect the adulteration types under diverse real-world conditions.

TABLE IV

ADULTERANTS AND THEIR CONCENTRATIONS IN OUR COLLECTED DATASET. SIX COMMON TYPES OF ADULTERATION AND 13 DIFFERENT ADULTERANTS WITH EACH CONTAINING TWO CONCENTRATIONS ARE CONSIDERED.

Types	Adulterants	Concentration
Substitute	Pork	10%, 50%
	Chicken	10%, 50%
	Duck	10%, 50%
Dye Substitute (Color & Essence)	Pork	10%, 50%
	Chicken	10%, 50%
	Duck	10%, 50%
Low Quality	Beef Offal	10%, 50%
Stale Beef		10%, 50%
Edible Additive	Vegetable Protein	5%, 20%
Water Injected	Water	5%, 20%
Toxic Additive	Antibiotic	(0.75, 3) ug/kg
	Stimulant	(0.3, 1.2) ug/kg
	Preservative	(0.15, 0.6) mg/kg

#### D. Meat Spectral Reconstruction Dataset Development

To achieve an effective data alignment, we design a pre-processing pipeline through image processing algorithms. The pipeline involves four steps to ensure that the MSI and HSI data are aligned and addresses challenges posed by ambient light influence, resolution differences, and variations in sample location during data collection. **(1) Elimination of Ambient Light.** In real-world scenarios, the uncontrollable intensity of environmental illumination may hinder learning a reliable reconstruction mapping. To overcome this, we apply background subtraction by removing the spectral image illuminated solely by ambient light. This eliminates the environmental illumination and improves the accuracy of subsequent analysis. **(2) Median Filtering and ROI Extraction.** To enhance the quality of the selected images, we employ median filtering to reduce noise. Additionally, for meat samples placed in circular petri dishes, we utilize the Hough Circle Transform [33] to extract the regions of interest (ROI). To achieve angle alignment of the extracted ROIs, we stick a black circular marker on each petri dish and rotate ROIs so that the marker centers are aligned. This approach compensates for variations in sample location and ensures accurate analysis. **(3) Spatial Alignment.** After cropping the images, we observe a resolution difference between the MSI and HSI images. To address this, we down-sample the larger image using nearest neighbor interpolation, ensuring they have the same size. Then by aligning the marker and meat centers along a vertical line, we eliminate misalignment and ensure accurate correspondence between MSI and HSI pairs. **(4) Central Area Extraction.** To focus on the most informative regions, we extract central areas of  $320 \times 320$  pixels from the aligned MSI and HSI cubes. This enables efficient analysis and reduces computational complexity while preserving essential information for further processing.

Based on this pre-processing pipeline, we collect a spectral reconstruction dataset for minced beef adulteration inspection. Table IV illustrates the adulteration types in our dataset. Based on the survey of various types of adulteration and their frequency in developing countries [21] and their harmfulness,

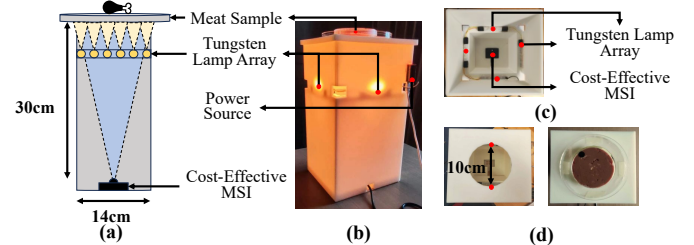


Fig. 11. Prototype of MeatSpec, which cost <\$60. Users can finish adulteration detection by simply placing the meat sample at the top of the box.

we define six common types of adulteration. For each type of adulteration, we select several typical adulterants, resulting in a total of 13 different adulterants. Each adulterant is used at two concentrations, including a minimum adulteration concentration and a typical adulteration concentration<sup>1</sup>. The concentrations are set with reference to various surveys and standards [34], [35], [36]. We produce three samples for each adulterant and scan collect four (MSI, HSI) images for each sample. Overall, a total of 347 paired MSI and HSI images are collected, which can be accessed in [22].

Furthermore, our dataset can be expanded to include samples of other adulterated meats for a wider scope of meat adulteration detection, not limited to beef samples. The AOSR and RAAD modules do not need any changes.

## IV. IMPLEMENTATION

We implement a compact and low-cost prototype using off-the-shelf multispectral camera (named Monarch [15]) and light components. As shown in Figure 11, the prototype is a semi-enclosed 3D printed box using white resin. The multispectral camera is placed at the bottom of the box with the lens facing up. Users can finish sample scanning by simply placing the meat sample at the top of the box. To capture one image, it takes about 750ms.

**Multispectral Camera.** Monarch has two advantages over other commercial multispectral cameras on the market that prompt us to choose it. First, most low-cost multispectral cameras on the market only cover visible light [26], but Monarch operates at frequencies ranging from 690nm to 950nm in the near-infrared band, providing more spectral features relevant to meat adulteration detection. Second, it's cheaper, Monarch uses the novel MEMS spectral imaging chip based on Fabry-Perot broadband filter to dramatically reduce the cost of hardware, which costs around \$50 for mass production. In addition, Monarch can report real-time camera temperatures during image capturing. If long-term operations are needed, we can calibrate the camera's MSI wavelengths according to the linear relationship between wavelength shift of Fabry-Perot filter and temperature changes [37]. Practically, this situation rarely happens because our system latency is <1.5 seconds (see §V-B3) with no need for long-time operations. An

<sup>1</sup>For example, the "10%, 50%" indicates the 1:9 or 5:5 mass ratio of the adulterant to the beef. The "(0.75, 3) ug/kg" means that the 0.75 ug/kg or 3 ug/kg concentration additives are prepared and sprayed on the surface of the beef sample.

TABLE V  
COMPARING THE PARAMETERS OF THE MSI AND HSI CAMERAS USED IN OUR EXPERIMENT.

Parameters	Cubert (HSI)	Monarch (MSI)
Spectral Range	450-1000 nm	690-950nm
Spatial Size	1000×1000 pixels	1280×1024 pixels
Band Num	138	10
Wavelength (nm)	[450:1000::4] (i.e., 450, 454, 458, 462, ..., 1000)	713, 736, 759, 782, 805, 828, 851, 874, 897, 920
Cost	> \$10,000	≈\$50

automatic, built-in one-time calibration before image capturing is enough for practical usage.

**Light Source.** We need to ensure sufficient light intensity at the sample to produce clear multispectral images. To this end, we place 12 full-band tungsten lamps (VCC7216-ND) at a distance of 10cm from the top of the box. All the lamps are connected in parallel and powered by a teensy@4.0 development board [38]. In addition, To ensure uniform illumination distribution, as shown in Figure 11 (c), the 12 lamps are uniformly placed at the four walls of the box.

Our prototype can support ubiquitous usage due to its low cost (<\$60), portability and generalizability, suitable for end-of-chain nodes' scenarios such as school cafeterias, catering institutions. Despite our system requires illumination and extra MSI device instead of a smartphone, it can achieve accurate meat adulteration detection which smartphone's three-channel RGB images cannot achieve.

## V. PERFORMANCE EVALUATION

### A. Study Setup

1) *Training Scheme:* As mentioned in § III-D, the paired HSI and MSI in our dataset both have 320×320 pixels after processing. To train the AOSR model, we split the images into 64×64 patches, with a batch size of 32, an initial learning rate of  $10^{-4}$ , and a cosine preselection annealing decline to  $10^{-6}$ . The model converges with a loss function weight ( $\alpha$ ) of 0.95 after 20000 iterations. To train the RAAD model, we use a batch size of 64, a distillation weight ( $\beta$ ) of 0.8, an initial learning rate of  $5 \times 10^{-4}$ , and cosine preselection annealing with a rate of  $10^{-6}$ . After training 1000 epochs, to prevent falling into a local optimum under cosine annealing, we reset the learning rate to a constant value of  $5 \times 10^{-5}$  and continue training the model with additional 1000 epochs. The RAAD classification model converges to the final result after 2000 epochs.

2) *Metrics:* We reformulate the meat adulteration inspection task into a multi-classification task, which not only should distinguish the adulterated sample from the authentic sample but also detect the adulteration types. Multi-classification is essential because 1) the health risks and responses to different types of adulteration are completely different, e.g., the risk of toxic additives is very high and requires prompt medical attention; 2) for ubiquitous scenarios such as school cafeterias or catering institutions, it is not only necessary to determine whether a meat sample is edible but also to trace the source of adulteration and manage the supply chain according to

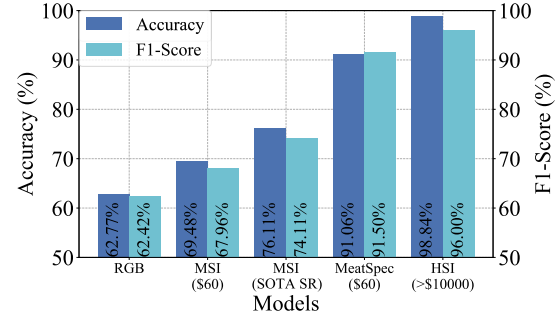


Fig. 12. Stratified 5-fold cross-validation performance comparison between MeatSpec and baselines.

the specific adulteration types. As depicted in § III-D, we consider six common types of adulteration. Thus, we have 7 classes in total, including authentic beef (0), substitution (1), dye substitution (2), low-quality meat (3), edible additives (4), water injection (5), and toxic additives (6). To evaluate the performance of meat adulteration multi-classification task, we exploit the **Macro-averaging Accuracy** and **F1 score** as the metrics.

3) *Baselines:* We compare our system's performance with several baselines. (i) *RGB*. We use the corresponding RGB images generated by the captured HSI to conduct the classification. We build a ResNet [39] network to classify the generated RGB images. (ii) *MSI*. We directly use MSI images for classification. We use random forest and CNN, which are typically used in previous works [40], to classify the spectra that averaged in spatial dimension. We choose the better result from random forest and CNN for this baseline. The first two baselines are end-to-end deep learning-based detection without spectral reconstruction. (iii) *MSI (SOTA SR)*. We use the existing SOTA spectral reconstruction algorithm [16] to reconstruct the HSI, and then use random forest and CNN to classify the spectra according to the conventional methods [40]. Similarly, we choose the higher performance from random forest and CNN. Due to the cross-band reconstruction errors, here using CNN tends to model overfitting and the random forest's performance is slightly higher. (iv) *HSI*. We use hyperspectral data collected by an expensive HSI camera [27] for classification, and use our designed CNN classifier. Tabel V shows more detailed parameters of the HSI camera comparing with our MSI camera. Note that although the performance of MeatSpec is supposed to be inferior to this baseline, MeatSpec far outperforms this solution in terms of price.

### B. Overall Performance

We first evaluate MeatSpec's performance on different adulteration type detection by conducting stratified 5-fold cross validation<sup>2</sup>, by which the ratio between the target classes is the same in each fold as it is in the full dataset.

1) *Baselines Comparison:* Figure 12 compares the accuracy and F1-score of our MeatSpec with baselines, revealing three important findings. Firstly, using unmodified MSI or RGB for adulteration detection results in poor performance, with less than 70% accuracy, due to their limited and coarse-grained

<sup>2</sup>Doing stratified cross-validation can ensure that the cross-validation result is a close approximation of generalization error.

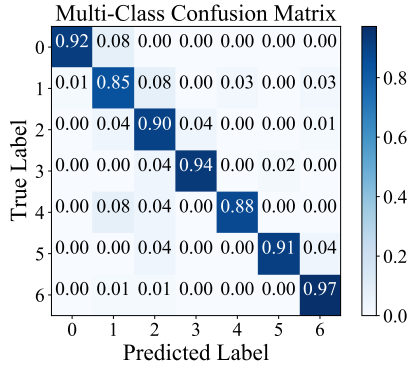


Fig. 13. Confusion matrix of MeatSpec on multiple meat adulteration types detection

spectral information. Secondly, applying the existing SOTA SR algorithm to MSI only slightly improves the system's performance, since it fails to recover fine-grained differences and combat reconstruction errors in reconstructed HSI, leading to low classification accuracy. Finally, our designed system achieves 91.06% accuracy for the meat adulteration type detection task, which is 21.58% higher than that of the direct use of MSI and 14.95% higher than that of the MSI using the existing reconstruction algorithm, demonstrating the effectiveness of the system design.

2) *MeatSpec's Performance*: Figure 13 and Figure 14 present the confusion matrix and AUC-ROC curve of MeatSpec for detecting multiple meat adulteration types, respectively. We can observe the consistently good performance of MeatSpec across all adulteration types. Notably, MeatSpec can accurately distinguish authentic beef samples from adulterated samples, achieving an accuracy of 92%, even with various types of adulteration. Moreover, we conduct two-dimensional t-distributed stochastic neighbor embedding (t-SNE) projections [41] to illustrate the embedding representations of MeatSpec. Figure 15 displays our results, which indicate that MeatSpec displays clear clustering of all classes, demonstrating its aptitude for identifying various adulteration types.

3) *System Overhead and Time Latency*: We use NVIDIA T4 Tensor Core GPU to testify our models' time latency and overhead. For our AOSR module, the total parameter number of the reconstruction model is 4.14M with 512.67G floating-point operations per second (FLOPs). The inference latency of reconstructing one meat sample's MSI is 665.4ms on average. For our RAAD module, its regression model' total parameter number is 0.92M with 0.376G FLOPs and 1.87ms inference latency on average. Both two modules could be deployed on the server side for fast inference, where the latency could be further reduced if more effective GPUs like A100 are employed. Overall, the full system latency is less than 1.5 seconds including image capturing, which is low and acceptable for daily usage.

### C. Ablation Study

We then investigate the modules of MeatSpec by conducting ablation study to demonstrate the effectiveness of the system design.

1) *Effectiveness of Application-oriented Spectral Reconstruction*: From the results shown in Table 16, we can find that by introducing AOSR scheme, the system improves about 7.76% accuracy than the baseline, which indicates its effectiveness of gaining more spectral features related to adulteration types. Specifically, by involving adulteration prior information and contrastive loss, the distance between the selected sample and the samples of other adulteration classes is increased, thus helping the reconstruction model to learn the nuances between the adulteration samples of different classes.

2) *Effectiveness of Reconstruction-adapted Adulteration Detection*: The effectiveness of the RAAD structure is reflected in the results of Table 16, which show an accuracy improvement of 11.25% compared to the baseline. This structure enhances the model's recognition ability in two ways. Firstly, it extracts more information from the visible light band to compensate for the large reconstruction error of the reconstructed data. Secondly, by narrowing down the features of the HSI and reconstructed images, the model learns a feature space that is more similar to the HSI feature, thereby improving classification performance.

### D. Impacts on Experimental Conditions

We then evaluate MeatSpec under various experimental and environmental conditions, as shown in Figure 17. We conduct the experiments using beef and one typical adulteration type, *i.e.*, substitute. For each experimental condition, we prepare two authentic samples and two substitute adulteration samples containing 50% of pork. Each sample is scanned by our prototype back and front twice, thus introducing eight authentic images and eight adulteration images. Both the reconstruction model and classification model are trained using all data collected in normal experimental conditions.

1) *Varying Meat Size and Height*: Our system is designed to be flexible, allowing users to vary the amount of meat used for detection, which can affect the size, shape, and thickness of the sample. To test our system's performance, we create samples of four sizes and five thicknesses. The results are shown in Figure 18(a)-18(b). We find that the system is more robust to different sizes than thicknesses. This is because our system eliminates the influence of ambient light by collecting a background map before scanning the sample. While the thickness of the sample can impact the system's performance, we find that our system performs well when the sample thickness is more than 1cm. Since beef patties on the market are generally 1-2cm thick, our system can handle most situations with ease.

2) *Varying Meat Minced Size*: The physical structure of minced beef with different degrees of grinding is different, which will affect the reflection and scattering route of light. Thus, we set the meat grinder to four different mixing times, which directly decide the degrees of grinding. As can be seen from Figure 18(c), when the stirring time is less than one minute, the performance of the system is affected, especially the performance of the production sample is slightly reduced, which may be because the adulterants are not evenly mixed due to insufficient stirring. The spatial distribution of the

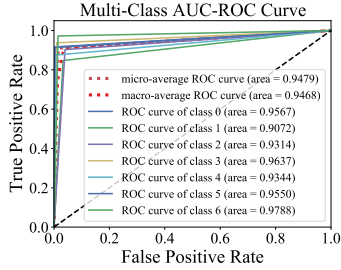


Fig. 14. AUC-ROC Curve of MeatSpec's result.

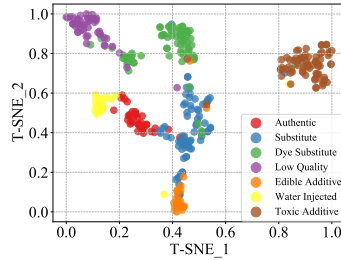


Fig. 15. T-SNE latent embedding distribution of MeatSpec's classification model.

Ablation Models	Accuracy	F1-Score
MSI (SR)	76.11%	74.11%
MeatSpec (w/o RAAD)	83.87%	81.86%
MeatSpec (w/o AOSR)	87.36%	87.09%
<b>MeatSpec (our)</b>	<b>91.06%</b>	<b>91.50%</b>

Fig. 16. MeatSpec's performance comparing with ablation models and different base reconstruction models.

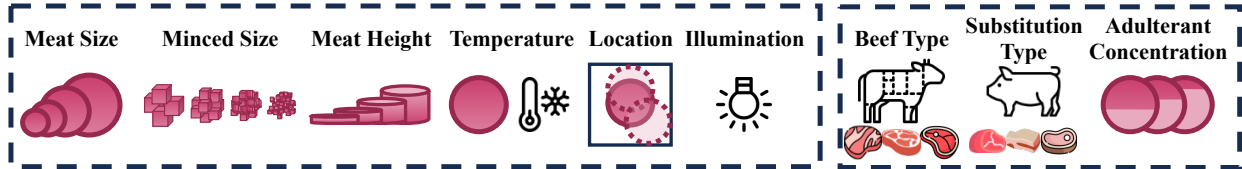


Fig. 17. Illustration of various experimental conditions.

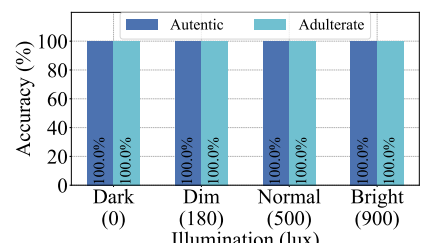
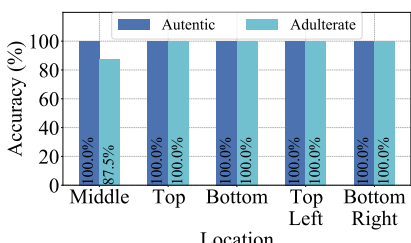
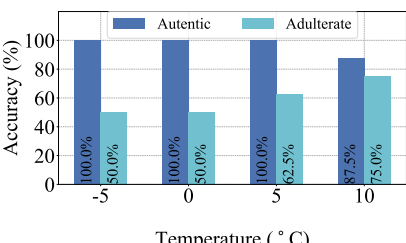
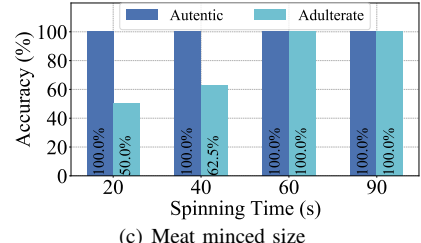
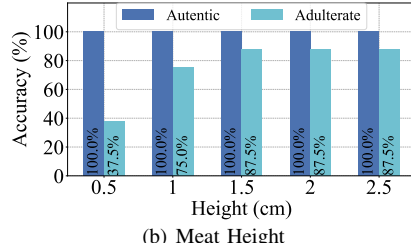
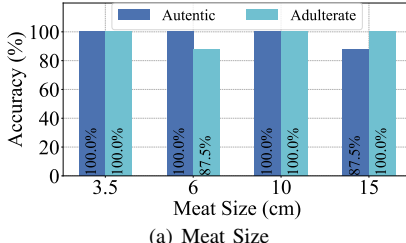


Fig. 18. MeatSpec performance under various experimental and environmental conditions.

collected MSI images is quite different from that of the fully mixed samples in the training set. This problem can be solved by calibrating the model using coarse-particle samples. While, when the samples are fully mixed and ground, the system can achieve good performance.

3) *Varying Meat Temperature*: The temperature of food affects its molecular thermal motions, which in turn affects the diffuse reflection of light. To evaluate MeatSpec under different food temperatures, we consider four common meat temperatures. The prepared samples are refrigerated at  $-18^{\circ}\text{C}$  for 8 hours and then thaw in normal temperature. Figure 18(d) reports the results, which indicate huge influence of temperature on our system. However, upon in-depth analysis of the classification results, we find that the misidentified samples are classified as either water-injected or low-quality substitution. This may be due to the precipitation of a lot of water in the process of refrigeration and thawing, and too long thawing time leads to the sample is not fresh. Additionally, the camera temperature would not affect the detection performance due to the automatic calibration before image acquisition.

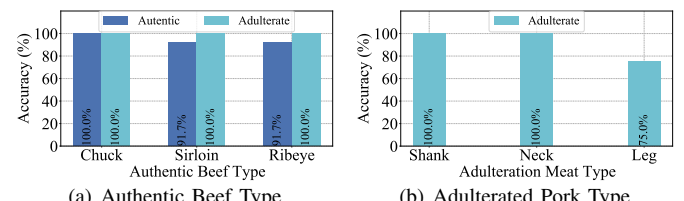


Fig. 19. MeatSpec performance on generalization to various experimental setups.

4) *Varying Sample Placement*: Since our light source does not illuminate the sample uniformly from the center but from four sides, the meat samples may be exposed to different intensity light sources when placed at different scanning positions on the top. To test the robustness of the system to different positions, we use 6cm samples placed in five different areas on the top. The results in Figure 18(e) show that our system is not sensitive to the placement of the samples. This may be attributed to our background elimination algorithm and the classification model's pooling process, which eliminates the

unevenness of the light field distribution

5) *Varying Ambient Illumination*: Ambient light can interfere with the readings of the MSI camera, which can negatively impact the performance of MeatSpec. Thus, we investigate the performance of MeatSpec under various realistic lighting conditions. We test the system under four different light settings. As shown in Figure 18(f), MeatSpec's performance is stable under different lighting conditions, as expected. This is because we place the camera at the bottom of the semi-closed box, blocking the majority of the ambient light, and utilize the proper background subtraction method.

6) *Varying Authentic Beef Type*: Minced beef on the market may be prepared using different types of beef. We select three representative beef parts, which are commonly used as raw materials for making ground beef<sup>3</sup>. We select a brand from a different origin for each part and calibrate the model using three parts of beef from one of the sources and then test it on samples from other sources. The results are shown in Figure 19(a). We can see that after calibration, the model also has good generalization performance for different parts of beef. If the users want to extend the model to more beef parts, only need to collect a small number of new parts of the sample to calibrate the model.

7) *Varying Adulteration Meat Type*: The same substitution class of adulteration may also include different kinds of substitutions, such as pork adulteration with different parts of pork. Therefore, taking pork adulteration as an example, we consider the adulteration of three different parts of pork. The model is also calibrated using a variety of pork parts, and Figure 19(b) shows the results on the remaining samples. As shown in the Figure 19(b), except for leg pork, the model has a good prediction performance for different parts of adulterated pork, and leg pork is incorrectly classified as the alternative category of crying dye, which may be caused by the rich content of myoglobin in leg pork.

8) *Multi-Type Adulteration*: We further evaluate MeatSpec's performance in predicting multiple types of adulterants simultaneously. We include five two-type mixed cases and two three-type mixed cases commonly found in real scenarios. The label of mixed cases included 1-2, 1-3, 1-4, 2-3, 2-4, 1-2-3, and 1-2-4. Each case involves mixing different adulterated samples with 50% concentration and creating one sample to fine-tune the classification model and multiple samples for testing. The model, trained on a single-type dataset, achieved an 86.48% F1-Score, with a 68.85% exact match ratio for multi-label and a 92.39% accuracy for each instance. These results demonstrate MeatSpec's effectiveness in detecting multiple types of adulterants by distinguishing their unique spectral characteristics, thanks to MeatSpec's ability to restore fine-grained spectral information.

## E. Generalizability

We then evaluate the effectiveness of our generalizability enhancement modules in § III-C.

<sup>3</sup>[https://en.wikipedia.org/wiki/Ground\\_beef](https://en.wikipedia.org/wiki/Ground_beef)

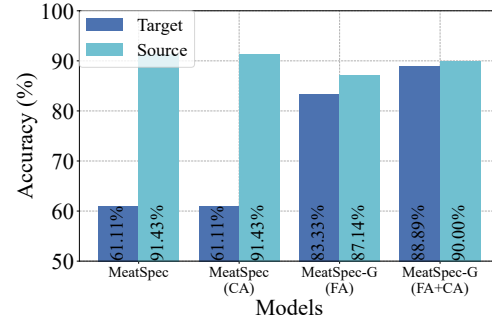


Fig. 20. MeatSpec-G's generalization performance on unknown adulteration conditions, comparing with ablation models and MeatSpec model. Here “Target” denotes the new samples of varied unknown adulteration conditions and “Source” denotes the previous samples of known adulteration conditions. “FA” denotes feature alignment and “CA” denotes channel attention aid.

1) *Varying Adulteration Conditions of Known Adulterants*: We evaluate MeatSpec-G under 20%, 30%, 40% concentrations of pork adulterants and pairwise combinations of pork, chicken and duck as admixture patterns. For each adulteration condition, we prepare three adulteration samples. To ensure the training samples contain different admixture patterns for conducting feature alignment, we also collect five adulteration samples of triple combinations of pork, chicken and duck, and add these data into the training set, which already contains the single-adulterant samples. Then, we retrain the MeatSpec model with feature alignment loss and obtain the MeatSpec-G model. As demonstrated in Figure 20, the classification accuracy of MeatSpec-G can reach 88.89% on unknown adulteration concentrations and admixture patterns, significantly outperforming the MeatSpec model in our conference version by 27.78%. For the previous MeatSpec model, the performance gap between known and unknown adulteration types is around 30% while this gap using MeatSpec-G model is decreased to only 1.1%. This is benefited from the enhanced feature similarity among diverse adulteration conditions for same-type adulterants, through our feature alignment module. Meanwhile, the accuracy of MeatSpec-G model on previous known meat samples can still maintain 90%, which demonstrates that MeatSpec-G model is not overfit with the balance of multi-task weights. Besides, from Figure 21, we can find that choosing an appropriate weight  $\gamma$  from 0.1 to 0.3 results in a satisfied performance, while a larger weight will lead to overfitting and a smaller weight will lose the effect of feature alignment, which needs to trade-off. Moreover, according to the ablation models' results, we can find that on the basis of feature alignment, employing channel attention to highlight the seen characteristic absorption peaks can further strengthen the generalizability and avoid overfitting. Note that merely using channel attention without feature alignment cannot alter the distribution of model features and thus does not bring performance gain. Overall, through our feature alignment module in MeatSpec-G, our model's generalization performance is greatly improved.

2) *Unknown Adulterants*: Additionally, to assess the cascaded open-set framework's ability to detect novel adulterants, we introduce two entirely new adulteration categories: starch

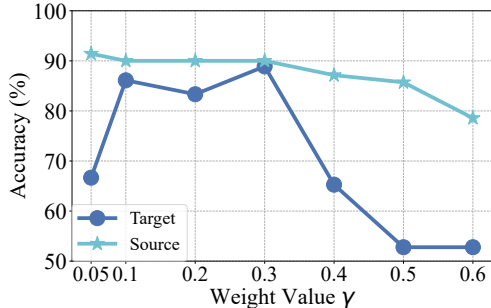


Fig. 21. MeatSpec-G's generalization performance under different weights of feature alignment ( $\gamma$ ).

TABLE VI  
PERFORMANCE COMPARISON ON UNKNOWN ADULTERANTS OF  
MEATSPEC-G AND BASELINES

Solution	Known Acc	Unknown Acc	F1-Score
MeatSpec	92.11%	0.0%	0.6236
MeatSpec (Softmax)	92.11%	31.25%	0.7414
MeatSpec (Energy)	88.16%	47.92%	0.7725
MeatSpec (Mahalanobis)	90.79%	72.92%	0.8435
<b>MeatSpec-G</b>	92.11%	83.33%	0.8792

and gelatin, which are unseen during model training. These additions expanded the test scope with 48 new MSI images (two concentrations with 5% and 20% per adulterant) beyond the original dataset. We use 80% of the data in original 347-image dataset to train the model and 20% of the data as validation dataset. The validation set is leveraged to calibrate optimal thresholds, including the energy score threshold  $\tau_{energy}$  and Mahalanobis distance threshold  $\tau_{mah}$ . As depicted in Table VI, the framework achieved an accuracy of 83.3% for unseen adulterants, which improves 31.25% over the solution based on softmax threshold. Moreover, we observe that MeatSpec-G maintains the same accuracy for known samples, demonstrating robust novelty detection without compromising closed-set accuracy. In addition, based on the ablation analysis results presented in Table VI, removing either stage significantly degraded performance. Firstly, the energy-only variant suffered a 35.4% drop in unknown detection due to overconfidence in ambiguous samples, while the Mahalanobis-only variant exhibited a 10.4% gap as reconstruction artifacts obscured discriminative features without Stage 1 filtering. Moreover, Figure 22 shows the joint distribution of energy score and Mahalanobis distance, revealing that both metrics exhibit ambiguous regions in classification, which necessitates combining them. This confirms the necessity of decoupling uncertainty quantification and anomaly discrimination to overcome the dual failure modes of overconfidence and spectral reconstruction bias.

## VI. RELATED WORK

In this section, we briefly review existing works related to meat adulteration detection, hyperspectral reconstruction algorithms and cost-effective spectral systems.

**Meat Adulteration Detection.** Various methods have been developed for detecting meat adulteration, each with its own advantages and limitations [42], [43]. Early detection methods [7], [8], [44], [9], offer accurate detection of animal DNA

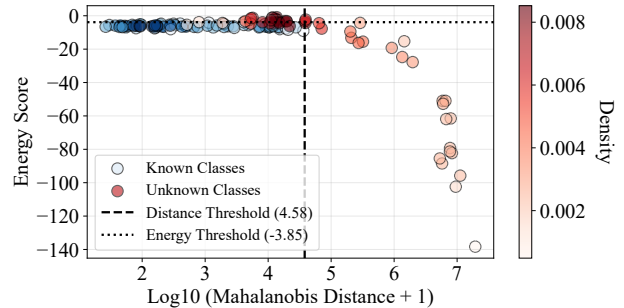


Fig. 22. Joint distribution of energy and log-distance on known and unknown samples.

compositions in meat products but often involve complex sample preparation procedures. Electronic noses and spectroscopy techniques [12], [10], [11] are capable of obtaining accurate results without sample preparation but require expensive equipment. Smartphone-based solutions only rely on visual features [45], [46], [13], [14] thus may struggle to scale up to more harmful adulteration scenarios involving excessive additives. In contrast, MeatSpec uses a reconstruction algorithm to improve the spectral granularity of the system, thus significantly reducing the cost of the system and can identify more adulterants.

**Hyperspectral Reconstruction Algorithms.** The idea of hyperspectral reconstruction is to reconstruct full hyperspectral data from limited spectral measurements, reducing the need for expensive and bulky hardware components. Conventional spectral reconstruction methods rely on hand-crafted hyperspectral priors [47], [48], [49]. Recently, deep learning techniques have been applied to learn the mapping function from RGBs to HSIs [20], [50], [28], [16], [19], [17]. However, these algorithms always ignore the deployment of reconstructed spectra in practical applications. In the context of meat adulteration detection, by combining advanced spectral reconstruction algorithms with application-specific adjustments, MeatSpec provides a more tailored and effective solution for meat adulteration detection.

**Cost-Effective Spectral System.** Spectral systems are valuable for substance identification but expensive, which always cost \$10,000, and inaccessible for many users. Researchers are working on making them more affordable and accessible. To address this, efforts have been made to simplify one-dimensional spectrometers using cheap LED and photodiode components [51], [52], [53], [54]. However, since lack of spatial-wise information, these systems can only work on liquid samples or homogeneous samples. Some systems use fewer components, sacrificing spectral resolution and requiring a large physical size [29]. There have also been efforts to use smartphones as spectral imaging systems, such as MobiSpectral [31], which focuses on the robustness of reconstructed spectra under different ambient light conditions. In contrast, MeatSpec operates in a semi-closed environment with minimal environmental interference, allowing it to focus on improving the quality of the reconstructed spectrum for fine-grained applications.

## VII. DISCUSSION

In this section, we will discuss the limitations and potential extensions of MeatSpec.

**Continual Reinforcement Learning.** Though our system has achieved a good generalization performance, the prediction error still exists. In practical uses, we can conduct continual reinforcement learning to constantly update the model and enhance its accuracy. Specifically, we can fine-tune our model according to the human feedback of the detection results, at regular intervals or whenever encountering abnormal adulterated samples. For example, if no adulterant is detected by our system but the user's taste experience is abnormal, or the sample is found as a problematic meat during government sampling inspection, we consider this detection result to be of low quality. We can exploit direct preference optimization algorithm in reinforcement learning to update our model based on high-quality and low-quality detection results.

**Hardware Selection.** Our paper expands the capability domain of low-cost spectral devices by using algorithms to distinguish samples with high similarity. If there is a similar performance but lower cost of multi-spectral hardware or better performance of spectral reconstruction algorithms, the framework of MeatSpec we designed can still be improved on alternative hardware and base reconstruction models. If future MSI cameras have more than ten frequency channels, wider channel ranges or no need for one-time calibration before image collection, using which the detection accuracy and time latency of our system can be further reinforced.

**Extension Applications.** Our solutions (AOSR and RAAD) can be easily applied to other meat adulteration, such as lamb adulteration. The basic rationales of restoring more distinguishable spectral images in AOSR and suppressing noise and error of full-band spectra in RAAD are not changed, and the mentioned six types of adulteration are universal. Furthermore, our proposed system has the potential to be used to solve other food adulteration problems, such as cereals and dairy products. By offering such a consumer solution for food adulteration detection, we can integrate these solutions into centralized dining settings to ensure the food safety of the users.

## VIII. CONCLUDING REMARKS

This paper presents MeatSpec, a consumer-grade spectral imaging system for meat adulteration inspection. MeatSpec simultaneously guarantees the fine-grained spectral capability required for meat adulteration detection and maintains a low-cost hardware setup. To achieve this, MeatSpec utilizes the existing spectral reconstruction technology and incorporates two novel modules, namely AOSR and RAAD. AOSR involves adulteration-related prior information and contrastive learning to reconstruct more easily distinguishable full-band hyperspectral images. RADD devises a CNN-based adulteration detection model based on the error distribution characteristics of the reconstructed HSI, and enhanced by knowledge distillation structure. Additionally, we reinforce the generalizability of our system and extend it to MeatSpec-G, by proposing a feature alignment-based training scheme to deal with varied adulteration conditions and a cascaded open-set recognition

framework to extend system capability on unseen adulterants. We also assemble an extensive dataset containing diverse adulterants. Experimental evaluations demonstrate that our system achieves a 91.06% accuracy in detecting multiple adulteration types, which surpasses the baseline performance without our proposed designs by 21.58%. Further, the system MeatSpec-G can generalize to unknown adulteration conditions and unknown adulterants, with a high detection accuracy of 88.89% and 83.33%, respectively.

## REFERENCES

- [1] T. N. A. L. Center, "The adulterating foodborne pathogens: Meat, poultry, and some egg products." <https://nationalaglawcenter.org/the-adulterating-foodborne-pathogens-meat-poultry-and-some-egg-products/>, 2023.
- [2] W. H. Organization, "Food safety." <https://www.who.int/news-room/fact-sheets/detail/food-safety>, 2022.
- [3] Q. Chang, W. Wang, G. Regev-Yochay, M. Lipsitch, and W. P. Hanage, "Antibiotics in agriculture and the risk to human health: how worried should we be?" *Evolutionary applications*, vol. 8, no. 3, pp. 240–247, 2015.
- [4] S.-H. Jeong, D. Kang, M.-W. Lim, C. S. Kang, and H. J. Sung, "Risk assessment of growth hormones and antimicrobial residues in meat," *Toxicological research*, vol. 26, pp. 301–313, 2010.
- [5] S. M. van Ruth and O. Nillesen, "Which company characteristics make a food business at risk for food fraud?," *Foods*, vol. 10, no. 4, p. 842, 2021.
- [6] R. S. Ahmad, A. Imran, and M. B. Hussain, "Nutritional composition of meat," *Meat science and nutrition*, vol. 61, no. 10.5772, pp. 61–75, 2018.
- [7] T. Notomi, H. Okayama, H. Masubuchi, T. Yonekawa, K. Watanabe, N. Amino, and T. Hase, "Loop-mediated isothermal amplification of dna," *Nucleic acids research*, vol. 28, no. 12, pp. e63–e63, 2000.
- [8] A. Pickar-Oliver and C. A. Gersbach, "The next generation of crispr–cas technologies and applications," *Nature reviews Molecular cell biology*, vol. 20, no. 8, pp. 490–507, 2019.
- [9] K. Nalazek-Rudnicka, I. Kłosowska-Chomiczewska, A. Wasik, and A. Macierzanka, "Mrm-ms of marker peptides and their abundance as a tool for authentication of meat species and meat cuts in single-cut meat products," *Food chemistry*, vol. 283, pp. 367–374, 2019.
- [10] H. Jiang, F. Cheng, and M. Shi, "Rapid identification and visualization of jowl meat adulteration in pork using hyperspectral imaging," *Foods*, vol. 9, no. 2, p. 154, 2020.
- [11] H. Jiang, W. Wang, H. Zhuang, S.-C. Yoon, Y. Yang, and X. Zhao, "Hyperspectral imaging for a rapid detection and visualization of duck meat adulteration in beef," *Food Analytical Methods*, vol. 12, pp. 2205–2215, 2019.
- [12] D. Karakaya, O. Ulucan, and M. Turkan, "Electronic nose and its applications: A survey," *International journal of Automation and Computing*, vol. 17, no. 2, pp. 179–209, 2020.
- [13] N. Seddaoui and A. Amine, "Smartphone-based competitive immunoassay for quantitative on-site detection of meat adulteration," *Talanta*, vol. 230, p. 122346, 2021.
- [14] W. Song, Y.-H. Yun, H. Wang, Z. Hou, and Z. Wang, "Smartphone detection of minced beef adulteration," *Microchemical Journal*, vol. 164, p. 106088, 2021.
- [15] Unispectral, "Unispectral monarch." <https://www.unispectral.com/product/monarch-nir-pcb/>, 2023.
- [16] J. Li, C. Wu, R. Song, Y. Li, and F. Liu, "Adaptive weighted attention network with camera spectral sensitivity prior for spectral reconstruction from rgb images," in *Proceedings of the IEEE/CVF Conference on Computer Vision and Pattern Recognition Workshops*, pp. 462–463, 2020.
- [17] Y. Zhao, L.-M. Po, Q. Yan, W. Liu, and T. Lin, "Hierarchical regression network for spectral reconstruction from rgb images," in *Proceedings of the IEEE/CVF Conference on Computer Vision and Pattern Recognition Workshops*, pp. 422–423, 2020.
- [18] Y. Cai, J. Lin, Z. Lin, H. Wang, Y. Zhang, H. Pfister, R. Timofte, and L. Van Gool, "Mst++: Multi-stage spectral-wise transformer for efficient spectral reconstruction," in *Proceedings of the IEEE/CVF Conference on Computer Vision and Pattern Recognition*, pp. 745–755, 2022.

- [19] Z. Shi, C. Chen, Z. Xiong, D. Liu, and F. Wu, "Hscnn+: Advanced cnn-based hyperspectral recovery from rgb images," in *Proceedings of the IEEE Conference on Computer Vision and Pattern Recognition Workshops*, pp. 939–947, 2018.
- [20] Z. Xiong, Z. Shi, H. Li, L. Wang, D. Liu, and F. Wu, "Hscnn: Cnn-based hyperspectral image recovery from spectrally undersampled projections," in *Proceedings of the IEEE International Conference on Computer Vision Workshops*, pp. 518–525, 2017.
- [21] X. Li, M. Zang, D. Li, K. Zhang, Z. Zhang, and S. Wang, "Meat food fraud risk in chinese markets 2012–2021," *npj Science of Food*, vol. 7, no. 1, p. 12, 2023.
- [22] MeatSpec, "Meatspec meat adulteration spectral reconstruction dataset." [https://drive.google.com/drive/folders/1mK7H9SZqEMkgJT3fQiuVL2PQwpw85r2m?usp=drive\\_link](https://drive.google.com/drive/folders/1mK7H9SZqEMkgJT3fQiuVL2PQwpw85r2m?usp=drive_link), 2024.
- [23] H. Hu, Y. Zhu, B. Yang, H. Kang, S. Chen, and Q. Zhang, "Meat-spec: Enabling ubiquitous meat fraud inspection through consumer-level spectral imaging," in *Proceedings of the 30th Annual International Conference on Mobile Computing and Networking*, pp. 861–874, 2024.
- [24] W. Wang and J. Paliwal, "Near-infrared spectroscopy and imaging in food quality and safety," *Sensing and instrumentation for food quality and safety*, vol. 1, pp. 193–207, 2007.
- [25] L.-C. Fengou, A. Lianou, P. Tsakanikas, F. Mohareb, and G.-J. E. Nychas, "Detection of meat adulteration using spectroscopy-based sensors," *Foods*, vol. 10, no. 4, p. 861, 2021.
- [26] SEETRUM, "Seetrum." <https://www.seetrum.com/>, 2024.
- [27] C. GmbH, "Fireflye 185." <https://www.cubert-hyperspectral.com/products/fireflye-185>, 2023.
- [28] A. Alvarez-Gila, J. Van De Weijer, and E. Garrote, "Adversarial networks for spatial context-aware spectral image reconstruction from rgb," in *Proceedings of the IEEE international conference on computer vision workshops*, pp. 480–490, 2017.
- [29] M. Goel, E. Whitmire, A. Mariakakis, T. S. Saponas, N. Joshi, D. Morris, B. Guenter, M. Gavriliiu, G. Borriello, and S. N. Patel, "Hypercam: hyperspectral imaging for ubiquitous computing applications," in *Proceedings of the 2015 ACM International Joint Conference on Pervasive and Ubiquitous Computing*, pp. 145–156, 2015.
- [30] M. Kamruzzaman, Y. Makino, and S. Oshita, "Rapid and non-destructive detection of chicken adulteration in minced beef using visible near-infrared hyperspectral imaging and machine learning," *Journal of Food Engineering*, vol. 170, pp. 8–15, 2016.
- [31] N. Sharma, M. S. Waseem, S. Mirzaei, and M. Hefeeda, "Mobicpectral: Hyperspectral imaging on mobile devices," in *Proceedings of the 29th Annual International Conference on Mobile Computing and Networking*, pp. 1–15, 2023.
- [32] A. Watson, C. Kendell, A. Lingamoorthy, I. Lee, and J. Weimer, "Lumos: An open-source device for wearable spectroscopy research," *Proceedings of the ACM on Interactive, Mobile, Wearable and Ubiquitous Technologies*, vol. 6, no. 4, pp. 1–24, 2023.
- [33] R. O. Duda and P. E. Hart, "Use of the hough transformation to detect lines and curves in pictures," *Communications of the ACM*, vol. 15, no. 1, pp. 11–15, 1972.
- [34] Food and A. Organization, "Faolex database." <https://www.fao.org/faolex/results/details/fr/c/LEX-FAOC176367/>, 2022.
- [35] R. Jiang, J. Shen, X. Li, R. Gao, Q. Zhao, and Z. Su, "Detection and recognition of veterinary drug residues in beef using hyperspectral discrete wavelet transform and deep learning," *International Journal of Agricultural and Biological Engineering*, vol. 15, no. 1, pp. 224–232, 2022.
- [36] Z. Huang, B. Li, S. Wang, R. Zhu, X. Cui, and X. Yao, "Robust and accurate classification of mutton adulteration under food additives effect based on multi-part depth fusion features and optimized support vector machine," *Food Analytical Methods*, vol. 16, no. 5, pp. 933–946, 2023.
- [37] W. Sheng, H. Lou, J. Pan, J. Wen, and G. Peng, "Online temperature drift compensation of fabry-perot filter based on machine learning and linear fitting," *Sensors and Actuators A: Physical*, vol. 363, p. 114774, 2023.
- [38] PJRC, "teensy40." <https://www.pjrc.com/store/teensy40.html>, 2022.
- [39] K. He, X. Zhang, S. Ren, and J. Sun, "Deep residual learning for image recognition," in *Proceedings of the IEEE conference on computer vision and pattern recognition*, pp. 770–778, 2016.
- [40] Z. Kang, Y. Zhao, L. Chen, Y. Guo, Q. Mu, and S. Wang, "Advances in machine learning and hyperspectral imaging in the food supply chain," *Food Engineering Reviews*, vol. 14, no. 4, pp. 596–616, 2022.
- [41] L. Van der Maaten and G. Hinton, "Visualizing data using t-sne," *Journal of machine learning research*, vol. 9, no. 11, 2008.
- [42] J. Du, M. Gan, Z. Xie, C. Zhou, M. Li, M. Wang, H. Dai, Z. Huang, L. Chen, Y. Zhao, et al., "Current progress on meat food authenticity detection methods," *Food Control*, p. 109842, 2023.
- [43] Q. Zia, M. Alawami, N. F. K. Mokhtar, R. M. H. R. Nhari, and I. Hanish, "Current analytical methods for porcine identification in meat and meat products," *Food chemistry*, vol. 324, p. 126664, 2020.
- [44] R. M. Lequin, "Enzyme immunoassay (eia)/enzyme-linked immunosorbent assay (elisa)," *Clinical chemistry*, vol. 51, no. 12, pp. 2415–2418, 2005.
- [45] W. Song, N. Jiang, H. Wang, and J. Vincent, "Use of smartphone videos and pattern recognition for food authentication," *Sensors and Actuators B: Chemical*, vol. 304, p. 127247, 2020.
- [46] J. Müller-Maatsch and S. M. van Ruth, "Handheld devices for food authentication and their applications: A review," *Foods*, vol. 10, no. 12, p. 2901, 2021.
- [47] B. Arad and O. Ben-Shahar, "Sparse recovery of hyperspectral signal from natural rgb images," in *Computer Vision–ECCV 2016: 14th European Conference, Amsterdam, The Netherlands, October 11–14, 2016, Proceedings, Part VII 14*, pp. 19–34, Springer, 2016.
- [48] Y. Fu, Y. Zheng, L. Zhang, and H. Huang, "Spectral reflectance recovery from a single rgb image," *IEEE Transactions on Computational Imaging*, vol. 4, no. 3, pp. 382–394, 2018.
- [49] Y. Li, C. Wang, and J. Zhao, "Locally linear embedded sparse coding for spectral reconstruction from rgb images," *IEEE Signal Processing Letters*, vol. 25, no. 3, pp. 363–367, 2017.
- [50] Y. Yan, L. Zhang, J. Li, W. Wei, and Y. Zhang, "Accurate spectral super-resolution from single rgb image using multi-scale cnn," in *Pattern Recognition and Computer Vision: First Chinese Conference, PRCV 2018, Guangzhou, China, November 23–26, 2018, Proceedings, Part II 1*, pp. 206–217, Springer, 2018.
- [51] Q. Huang, Z. Yang, and Q. Zhang, "Smart-u: smart utensils know what you eat," in *IEEE INFOCOM 2018–IEEE Conference on Computer Communications*, pp. 1439–1447, IEEE, 2018.
- [52] H. Matsui, T. Hashizume, and K. Yatani, "Al-light: An alcohol-sensing smart ice cube," *Proceedings of the ACM on interactive, mobile, wearable and ubiquitous technologies*, vol. 2, no. 3, pp. 1–20, 2018.
- [53] Y. Huang, K. Chen, L. Wang, Y. Dong, Q. Huang, and K. Wu, "Lili: liquor quality monitoring based on light signals," in *Proceedings of the 27th Annual International Conference on Mobile Computing and Networking*, pp. 256–268, 2021.
- [54] H. Hu, Q. Huang, and Q. Zhang, "Babynutri: A cost-effective baby food macronutrients analyzer based on spectral reconstruction," *Proceedings of the ACM on Interactive, Mobile, Wearable and Ubiquitous Technologies*, vol. 7, no. 1, pp. 1–30, 2023.